LANGMUIR

pubs.acs.org/Langmuir Article

Growth of Multilayers of Ionic Liquids on Au(111) Investigated by Atomic Force Microscopy in Ultrahigh Vacuum

Manuel Meusel, Matthias Lexow, Afra Gezmis, Andreas Bayer, Florian Maier, and Hans-Peter Steinrück*

Cite This: *Langmuir* 2020, 36, 13670−13681 Read Online

ACCESS | Metrics & More | Article Recommendations | Supporting Information

ABSTRACT: Understanding the growth of ultrathin films of ionic liquids (ILs) on metal surfaces is of highest relevance for a variety of applications. We present a detailed study of the growth of the wetting layer and successive multilayers of 1,3-dimethylimidazolium bis-[(trifluoromethyl)sulfonyl]imide ($[C_1C_1Im][Tf_2N]$) on Au(111). By atomic force microscopy (AFM) in ultrahigh vacuum, we follow the temperature-dependent behavior between 110 and 300 K at defined coverages. We initially observe the formation of a wetting layer with a thickness of ∼0.37 nm with anions and cations arranged in a checkerboard structure. Stable AFM imaging up to 280 K allows us to follow the IL growing on top of the wetting layer in bilayers with an average thickness of ∼0.71 nm, that is, double the height of the wetting layer, in a bilayer-by-bilayer fashion. This growth behavior is independently confirmed from the surface morphology, as deduced from AFM and angle-resolved X-ray photoelectron spectroscopy. High-resolution AFM images at 110 K allow for identifying the molecular surface structure of the bilayers as a striped phase, which is one of the phases also seen for the wetting layer (Meusel, M.; Lexow, M.; Gezmis, A.; Schotz, S.; Wagner, M.; Bayer, A.; Maier, F.; Steinrück, H. P. Atomic Force and Scanning Tunneling Microscopy of Ordered Ionic Liquid Wetting Layers from 110 K up to Room Temperature. *ACS Nano* **2020**, *14*, 9000−9010).

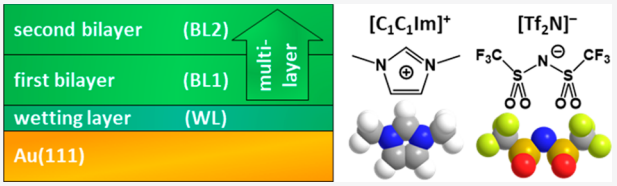

INTRODUCTION

Ionic liquids (ILs) have received increasing scientific attention within the last two decades.[1−4] They are mostly organic salts, characterized by a low melting point, often even below room temperature (RT). Their typically very low vapor pressure[5] enables applications in ultrahigh vacuum (UHV).[6−9] The ability to combine specific anions and cations by adequate synthesis and the option to also use mixtures allows for great tunability of the IL properties.[10,11] Together with their unique status within the available material classes, this renders ILs valuable for applications like lubrication,[12−14] separation,[15−19] electrochemistry,[20−30] and catalysis.[31−41] In the context of catalysis, two successful concepts, namely, supported ionic liquid phase (SILP)[36−38] and solid catalyst with ionic liquid layer (SCILL),[39] have been introduced. Both are based on a porous support material which is covered by a thin nonvolatile IL film. In SILP, a homogeneous catalyst is dissolved in the IL film, whereas in SCILL a heterogeneous catalyst (typically metal nanoparticles on a porous oxide support) is coated by the IL film. For all applications mentioned above, the IL/solid interface is highly relevant for the performance of the system. In particular, for SCILL, the IL/metal interface is of utmost importance, since the IL modifies the catalytic sites.[39,42,43] In order to tailor these systems for specific reactions, a detailed understanding of the IL/metal interactions, the IL film structure at the interface and in successive layers, the growth of ILs, and the dynamic behavior of the IL film is necessary.[4,42,44−48]

The properties of IL interfaces have been determined using various techniques. While the IL/vacuum interface has been investigated in detail using the methods of UHV-based surface science,[4,42,49−53] the IL/solid interface underneath thick IL films has been mostly addressed at ambient conditions, by methods which sufficiently penetrate the IL film. These include reflection absorption infrared spectroscopy (RAIRS),[54] sum-frequency generation,[55,56] X-ray or neutron reflectivity,[55,57] grazing incidence X-ray diffraction,[58] and electrochemical methods.[59−64] The corresponding studies permit conclusions on the orientation of ions at and layering near the IL/solid interface. Liquid-phase atomic force microscopy (AFM) and scanning tunneling microscopy (STM) offer an additional powerful route to study the IL/solid interface within a macroscopic IL droplet at ambient conditions. In particular, AFM force−distance measurements allow for determining layering effects and layer thicknesses,[2,65−80] even under an applied electrical potential. The majority of these studies were performed on Au(111) for ILs with imidazolium-based cations and $[Tf_2N]^-$ anions; they revealed layering of the ILs in the vicinity of the IL/Au interface, with layer thicknesses of around

Received: September 1, 2020
Revised: October 20, 2020
Published: November 6, 2020

https://dx.doi.org/10.1021/acs.langmuir.0c02596
Langmuir 2020, 36, 13670−13681

0.3−0.9 nm, depending on the individual IL.[2,67−78] Within these studies, the first layer in contact with the solid is sometimes thinner than the successive layers.[71,73−78] In addition, there exist numerous molecular dynamic simulations without and with applied electric potential, which address the adsorption geometry and layering effects of various ILs, mostly at metal surfaces.[81−86]

An alternative approach to study the IL/support interface is to investigate the properties of ultrathin (<5 nm) IL films on well-defined single-crystal surfaces under ultraclean conditions in UHV as recently reviewed by Lexow et al.[87] The films are typically deposited in situ using physical vapor deposition.[88,89] Working in UHV requires a significantly more complex experimental setup but has the advantage that the investigations are less prone to contamination effects. In particular, the water content in an IL has been shown to influence the interfacial structure on Au(111) and other surfaces like mica.[68,69,74,90−92]

Studies of the growth of IL films in UHV are mostly performed by angle-resolved X-ray photoelectron spectroscopy (ARXPS; see ref 87 and references therein), UV photoelectron spectroscopy (UPS),[93] and UHV-STM.[94−101] In particular, angle-resolved XPS has been proven to be very successful to study ion arrangement, multilayer growth, wetting behavior, and exchange phenomena in mixed IL films on various surfaces.[87] In 2011, a first ARXPS study on a single-crystal surface demonstrated that on Au(111) 1,3-dimethylimidazolium bis[(trifluoromethyl)sulfonyl]imide ($[C_1C_1Im][Tf_2N]$) and 1-methyl-3-octylimidazolium bis[(trifluoromethyl)-sulfonyl]imide ($[C_8C_1Im][Tf_2N]$) grow in a layer-by-layer fashion from submonolayer to multilayer coverage.[102] From the detailed analysis of the XP spectra it was concluded that in the first layer, the so-called wetting layer, anions and cations are in contact with the substrate forming a checkerboard-like structure of ∼0.37 nm thickness. This type of structure was later verified by UHV-based STM at temperatures of 240 K or lower for a variety of imidazolium- and pyrrolidinium-based ILs (see ref 87 and references therein). Very recently, our group demonstrated by UHV-based STM and UHV-based AFM that for $[C_1C_1Im][Tf_2N]$ this checkerboard structure is stable even at room temperature. At 110 K, striped or hexagonal superstructures coexist on the surface.[1] UHV-based STM studies, however, require stable tunneling conditions and only worked for coverages up to saturation of the wetting layer but not for successive layers, which would be required for studying the further growth and wetting behavior. At these higher coverages, stable STM imaging of topography and molecular resolution is challenging, even at very low temperatures of around 100 K.

Information on the growth behavior beyond the wetting layer can be derived from angle-resolved XPS. Depending on the combination of IL and substrate, very different modes were identified, from 2D layer-by-layer to pronounced 3D island growth (see ref 87 and references therein). A complementary but rarely used approach is helium atom scattering; one single in situ study for $[C_2C_1Im][Tf_2N]$ on Au(111) at 200 K showed that films grow in a layered fashion.[70] However, the authors did not observe a layered structure for coverages below the first three IL layers.

What is presently missing, however, is real space information on the structure of the IL during growth, that is, information on island sizes, ordered phases, and morphology. Herein, we present a UHV-based AFM study on the growth of $[C_1C_1Im][Tf_2N]$ on Au(111) in the temperature range from 110 to 300 K, from submonolayers to multilayers. The IL is deposited by physical vapor deposition (PVD) at low substrate temperatures (<170 K). During stepwise annealing up to 300 K, we monitor dynamic changes in the film structure. At 250 K, first a wetting layer is formed, with cations and anions in direct contact with the substrate, which is followed by IL growth in bilayers. This behavior is confirmed by angle-resolved XPS measurements at 300 K. For all layers, we are able to resolve on the molecular scale well-ordered domains of a very similar striped structure.

RESULTS AND DISCUSSION

The $[C_1C_1Im][Tf_2N]$ layers were prepared by PVD of a defined amount of IL onto a Au(111) single crystal at temperatures below 170 K in UHV. We used a specially modified IL evaporator with a very good long-time stability.[103] Each film was prepared on freshly cleaned Au(111) in the preparation chamber. After transfer to the AFM stage, it was measured by noncontact AFM at the denoted temperatures. The deposition rate was monitored in situ using a quartz crystal microbalance (QCM) positioned next to the crystal during the evaporation process. Its calibration is described in the Experimental Section. The IL dose required to achieve the coverage of a fully saturated wetting layer (= 1 WL) is denoted as one wetting layer equivalent (= 1 WLE). When plotting the surface coverage as obtained by AFM as a function of IL dose, we obtain a linear relationship (see SI Figure S1), which indicates that, at this temperature of the Au(111) crystal, the sticking coefficient of the IL is independent of the IL surface coverage. With this calibration, we are able to deposit well-defined amounts of IL in the coverage range from submonolayers to multilayers.

As an independent second method to study the growth behavior in the multilayer range, we measured the height profiles of the layers deposited on top of the wetting layer by AFM. Notably, this works exclusively in the multilayer range because the height of the islands can only be determined reliably if the chemical nature of the studied layers is identical, e.g., for an IL multilayer on top of the IL wetting layer. The step heights obtained this way are independent of the cantilever frequency shifts within our usual measurement window of $\Delta f = -150$ to -500 Hz (see Experimental Section). This approach, however, does not permit one to determine the step height of the wetting layer itself, since the force−distance curves of the metal substrate and the wetting layer islands are different, which for certain frequencies can even lead to negative height values. This ambiguity is the reason why no height profiles are shown for the WL. However, we estimate the height of the wetting layer with a checkerboard-like structure to be ∼0.37 nm from XPS.[102]

Figure 1 shows AFM images of $[C_1C_1][Tf_2N]$ on Au(111) in the coverage range up to a full wetting layer, that is, for IL doses up to ∼1 WLE. The IL was deposited at a substrate temperature below 170 K and measured at 110 (left AFM series), 200 (middle), and 300 K (right). The coverages (in WL), as obtained from the AFM images at 200 K, are denoted in the right upper corner of the 200 K images. Notably, they are obtained from a larger area than shown in Figure 1, that is, from several images, to obtain better statistics. The surface morphologies at 300 K are schematically sketched right of the corresponding 300 K images (Figure 1m−p).

https://dx.doi.org/10.1021/acs.langmuir.0c02596
Langmuir 2020, 36, 13670−13681

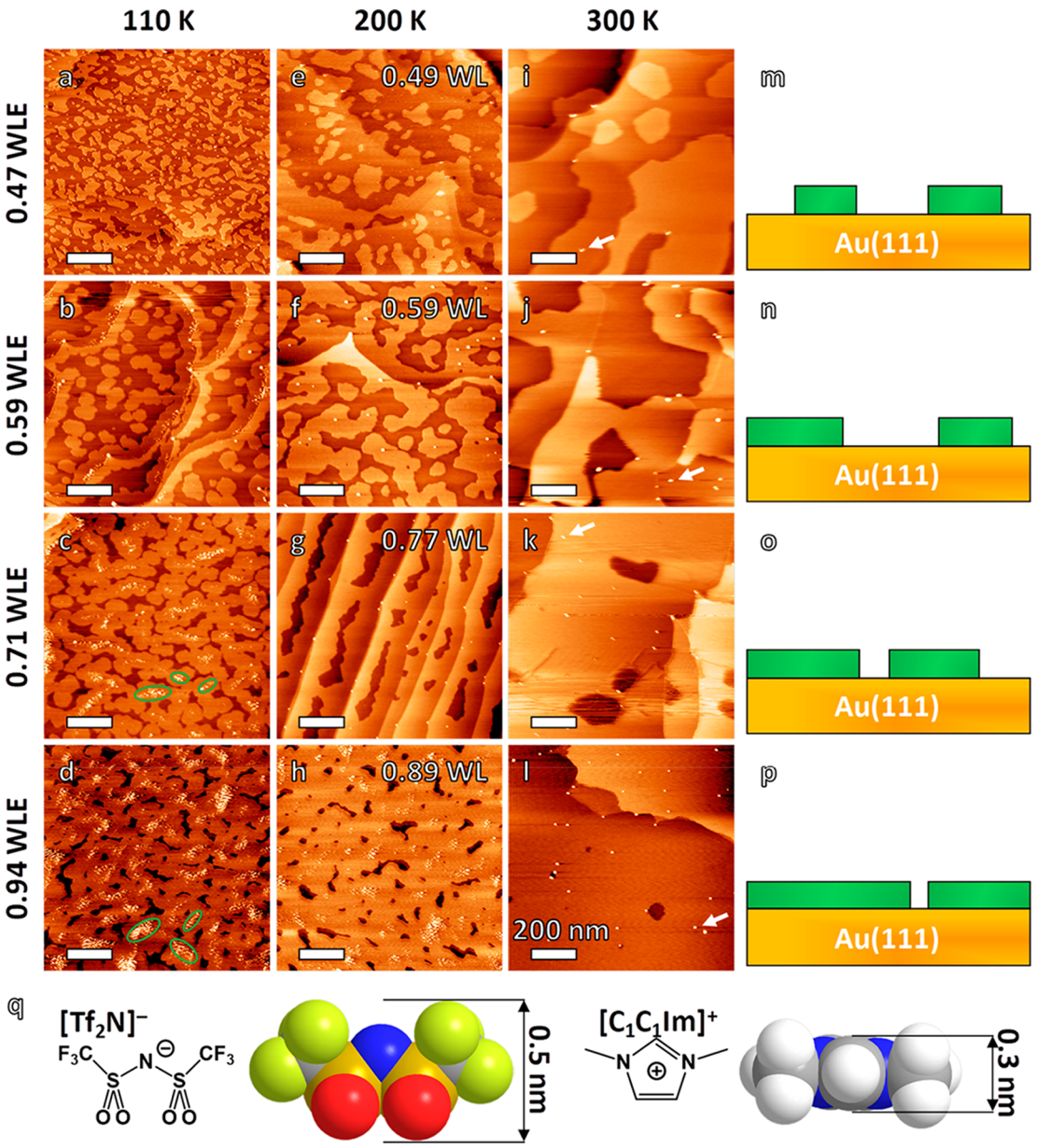

Figure 1. AFM images of sub-WL coverages of $[C_1C_1Im][Tf_2N]$ on Au(111), deposited at <170 K and measured at 110 (left), 200 (middle), and 300 K (right). The IL doses (in WLE) for a horizontal row are denoted left to the 110 K images, and the coverages (in WL) obtained from the AFM images at 200 K are denoted in the upper right corner of the 200 K images. In the images, a brighter appearance corresponds to a higher elevation. Initially, the IL forms flat wetting layer islands that ripen to larger islands with time at higher temperature. Starting at an IL dose of 0.71 WLE also small multilayer islands (indicated by green ellipses in c and d) form at a distance of roughly 50 nm to the next island edge. Arrows in i–l indicate bright spots, which likely are due to contaminations (see text). Details about the preparation and AFM parameters are given in the SI. In q, the chemical formula and a rough size estimation of the used ions are shown.

We start with discussing the data measured at 110 K. At low doses (Figure 1a), the IL forms islands on the Au substrate. Starting at an IL dose of 0.71 WLE (Figure 1c), we also find small multilayer islands (bright protrusions indicated by green ellipses in Figure 1c and 1d) in the center of the wetting layer islands with a distance of about 50 nm to the island edges. This behavior is attributed to a limited diffusion zone of the impinging IL ion pairs on top of the wetting layer while still being in a hot precursor state.[104] Ion pairs impinging within this zone can diffuse to the island edge and are incorporated there; ion pairs at a larger distance from the island edge form a multilayer island on top of the wetting layer islands. This growth behavior has been reported before.[105,106] For free-base tetraphenylporphyrin (2H-TPP) on Ag(111), e.g., Rojas et al. observed at 58 K the nucleation of a second layer of molecules on top of initial islands already before completion of the first layer.[107] In analogy to our study, the second-layer 2H-TPP molecules diffuse across the island boundaries upon heating and attach to the periphery of the first layer islands.

At 200 K, the wetting layer islands begin to ripen, forming large connected areas (Figure 1e and 1f). At larger coverages, uncovered areas appear as holes in the wetting layer (Figure 1g and 1h) with small multilayer islands still visible (Figure 1h). At 300 K, the ripening is even more pronounced and the multilayer islands have completely disappeared (Figure 1k and 1l). The fact that the multilayer islands disappear at a higher

https://dx.doi.org/10.1021/acs.langmuir.0c02596
Langmuir 2020, 36, 13670−13681

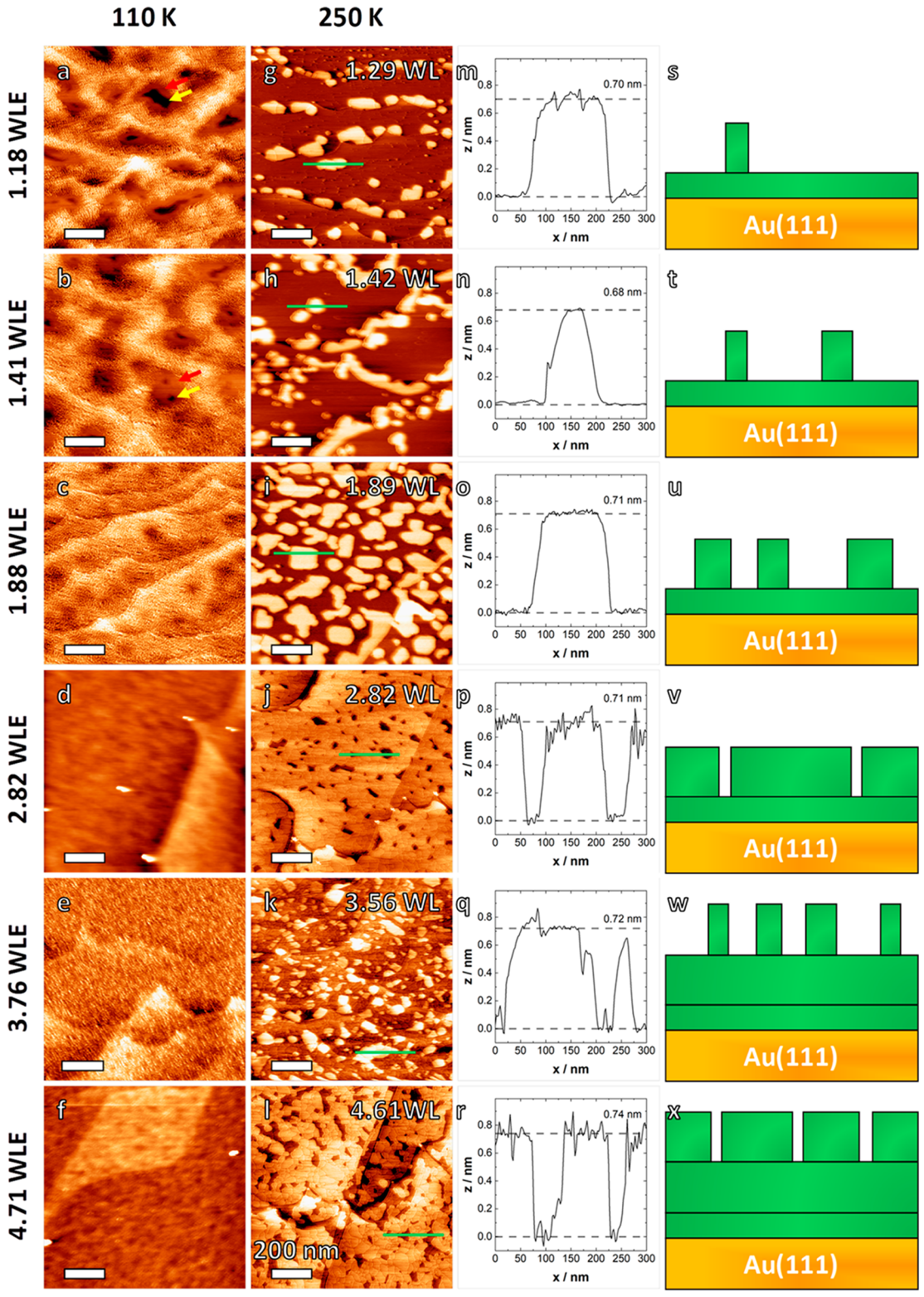

Figure 2. AFM images of multilayer coverages of $[C_1C_1Im][Tf_2N]$ on Au(111), deposited at <170 K and measured at 110 (left) and 250 K (right). The IL doses (in WLE) are denoted left to the 110 K images, and the coverages (in WL) obtained from the AFM images at 250 K are denoted in the upper right corner of the 250 K images. At low temperature, a wetting layer is formed with multilayer islands on top. While for IL doses up to 1.88 WLE (a–c) free metal surface is still present (black areas; yellow arrow), surrounded by ~50 nm wide multilayer-free space (dark areas, red arrow), at higher IL doses the surface is homogeneously covered with the small IL islands. During annealing, the wetting layer fills up and the small multilayer islands ripen to large flat islands. Height profiles obtained from the images at 250 K (green lines) show an island height of ~0.71 ± 0.05 nm which is twice the height of the wetting layer obtained from XPS. We thus conclude that the islands grow as bilayers (BL). AFM parameters are given in the SI.

https://dx.doi.org/10.1021/acs.langmuir.0c02596
Langmuir 2020, 36, 13670–13681

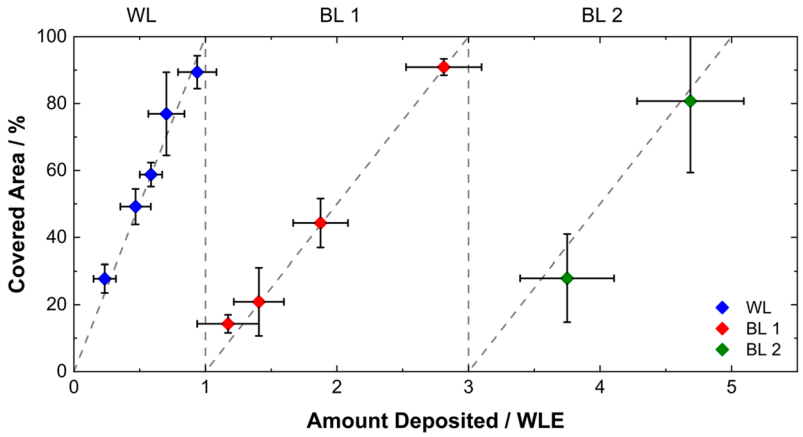

Figure 3. Covered area of the topmost layer of $[C_1C_1Im][Tf_2N]$ on Au(111) against IL dose in (WLE), calibrated with the microbalance. The denoted coverages are the average of several (3−8) AFM images measured at 200 or 250 K (see, e.g., Figures 1e−h and 2g−l, respectively). The dashed line serves as a guide to the eye. In the WL regime (blue symbols), the covered area increases linearly with IL dose and at 1 WLE the wetting layer is completed. The covered area on top of the wetting layer also follows a linear trend but with one-half the slope. For completion of one layer in the multilayer regime, 2 WLE are required. Therefore, the layers in the multilayer regime grow as bilayers, BL1 (red symbols) and BL2 (green symbols). Further details are given in Figures S1 and S4 in the SI.

temperature (or a later time, that is, when the sample was left in the chamber overnight at constant temperature) compared to the onset of the wetting layer ripening indicates a faster diffusion of IL ion pairs on the Au(111) surface than on the wetting layer islands. At the highest coverage, the wetting layer is nearly fully closed with a very homogeneous appearance (Figure 1l). The nature of the very few small protrusions (some are indicated by a white arrow) is not clear; likely, they are related to defects in the wetting layer.

In Figure 2, we display the AFM images of $[C_1C_1Im][Tf_2N]$ in the multilayer range, that is, after IL doses of 1.18 up to 4.71 WLE. The IL was deposited at a substrate temperature below 170 K and measured at 110 (left image series; Figure 2a−f) and 250 K (right image series; Figure 2g−l). The coverages (in WL), as obtained from the AFM images at 250 K, are denoted in the right upper corner of the 250 K images. In addition to the AFM images, we also highlight selected line scans (green lines in the images) along which we obtain the height profiles in Figure 2m−r. The surface morphology corresponding to the 250 K images is schematically sketched in Figure 2s−x.

At 110 K, we observe a rough and disordered image for all deposited layers with an appearance comparable to that of the multilayer islands observed in Figure 1, albeit with a much larger number of islands. At low multilayer coverage (Figure 2a and 2b) one can still see the ∼50 nm wide zones of a multilayer-free wetting layer (darker contrast, indicated by a red arrow) and holes with free metal surface (nearly black contrast, yellow arrow). With increasing amount of deposited IL (Figure 2c−f), the wetting layer is closing and the whole surface is covered with multilayer islands.

The appearance of the surface dramatically changes when heating to and measuring at 250 K (Figure 2, right image series). We chose this temperature, which is different from that in Figure 1, since at ∼200 K nearly no change is visible (see Figure S2c in the SI) and above 280 K reliable measurements of the IL multilayers with the AFM were not possible (for measurements at 300 K see Figure S2i in the SI). We believe that above 280 K, the multilayer IL becomes very mobile and frequently attaches to the AFM tip and accumulates there. Over the course of continued scanning, the tip eventually releases clumps of IL back to the surface (even after cooling down again; Figure S2g), which then interfere with the measurement. In addition, at 300 K, the coverage of the multilayers very slowly decreases (on the time scale of several hours; Figure S2j−l), which is likely due to multilayer desorption; this effect did not occur in the wetting layer measurements in Figure 1, because desorption from the wetting layer only occurs above 400 K.[1,87]

At 250 K (Figure 2, right image series), the deposited IL layers rearrange into flat islands or nearly closed flat films. The images were measured after at least 25 min at 250 K (for details see Table S1 in the SI) in order to ensure that the surface morphology did not show further changes with time. Overall, the system seems to tend toward maximizing the coverage of the lower (lowest) layers and minimizing the circumference of the islands in the topmost layer. The heights of the islands or holes average around 0.71 ± 0.05 nm for all depositions (BL1 = 0.69 ± 0.05 nm, BL2 = 0.72 ± 0.05 nm), as determined from line scans across island and hole edges (Figure 2m−r). The surface morphologies are in each case schematically sketched next to the corresponding height profiles (Figure 2s−x).

As a next step, we analyze the covered area in the 250 K images in Figure 2. At this temperature, the islands are sufficiently large for a reliable coverage determination (i.e., broadening effects at island edges are negligible; see Experimental Section for details). Interestingly, for an IL dose of 1.88 WLE (Figure 2c), that is, 0.88 WLE on top of the closed wetting layer, only about one-half of the wetting layer is covered by islands. Only for 2.82 WLE (Figure 2j) is a nearly closed second layer found. For 3.76 WLE (Figure 2k), a roughly half-filled third layer is found, and only at 4.71 WLE (Figure 2l), is a nearly closed full third layer seen. This behavior indicates that for the completion of further closed layers on top of the wetting layer, in each case about twice the amount of IL is required as for the wetting layer. This is visualized in Figure 3, where the covered area in the topmost layer (as determined by AFM) is plotted versus the amount of dosed IL (as determined by the QCM). While the formation of a complete wetting layer requires 1 WLE of deposited IL, the completion of the next two closed layers (BL1 and BL2) requires 2 WLE each; we therefore denote them as bilayers

https://dx.doi.org/10.1021/acs.langmuir.0c02596
Langmuir 2020, 36, 13670−13681

BL1 and BL2. Thus, after deposition of a total of 5 WLE the wetting layer plus two further bilayers are found on the surface. We thus conclude that the wetting layer grows as a single layer with anions and cations both in contact with the Au(111) surface and arranged in a checkerboard structure.[102] From that on the next layers grow as IL bilayers. Due to electrostatic reasons (see also discussion below), alternating pairs of anion and cation stacked vertically on top of each other are assumed in these bilayers. Notably, the growth of the multilayers in the form of bilayers is in perfect agreement with the line scans in Figure 2, which show a height of 0.71 ± 0.05 nm, which is about twice the height of 0.37 nm, as determined from XPS based on the checkerboard arrangement of cations and anions and the molar volume of the IL.[102]

Angle-resolved XPS has been used as a very powerful method to study the growth behavior of ILs on surfaces.[53,108] We thus performed a series of ARXPS measurements for $[C_1C_1Im][Tf_2N]$ on Au(111) at 300 K, which are in good agreement with the layer-by-layer growth observed here by AFM. Figure 4 shows the attenuation of the Au 4f substrate

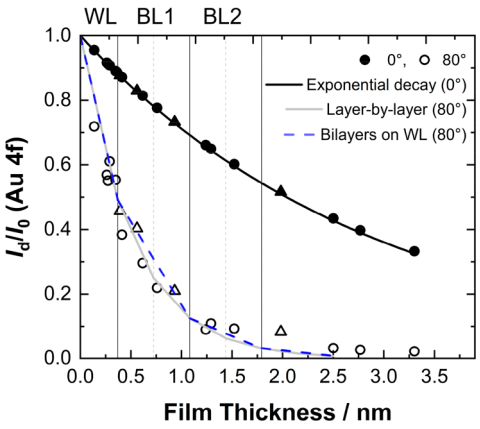

Figure 4. Attenuation of the Au 4f intensity obtained by ARXPS in 0° (full symbols) and 80° (open symbols) emission as a function of the film thickness d for $[C_1C_1Im][Tf_2N]$ on Au(111) at RT. The data from a previous study (circles)[102] and the data from this study (triangles) agree within the margin of the experimental error. For the 80° data, the solid gray and dashed blue lines indicate the section-wise linear decay for (1) 2D layer-by-layer growth with layer thicknesses Δd = 0.37 nm (like that of the wetting layer) and (2) 2D bilayer-by-bilayer growth on top of the wetting layer with Δd = 0.71 nm, as deduced from AFM, respectively. For 0°, the section-wise linear decays (not shown) can hardly be distinguished from an exponential function (solid black line, calculated with eq 1 with an inelastic mean free path, λ, of 3.0 nm[102]) and thus are not shown.

signal as a function of IL film thickness for electron emission angles of 0° (full symbols and black line) and 80° (open symbols). Due to the increased surface sensitivity (by a factor of 6), the signal at 80° is attenuated significantly stronger than that at 0°. The deposited amount of IL is determined from the data at normal emission (0°); for details, see the Experimental Section. For the 80° data, the solid gray and dashed blue lines indicate the section-wise linear decays for (1) layer-by-layer growth with layer thicknesses Δd = 0.37 (like that of the wetting layer) and (2) 2D bilayer-by-bilayer growth on top of the wetting layer with Δd = 0.71 nm (as deduced from AFM), respectively (notably, for 0°, the section-wise linear decays can hardly be distinguished from the solid black line and thus are not shown). While the experimental data points at 80° from two independent XPS experiments (circles from ref 102 and triangles from this work) are in good agreement, their scatter does, however, not allow for differentiating the two growth modes as detected by our UHV-AFM results. Nevertheless, the ARXPS data verify that the IL indeed grows in an overall layer-by-layer fashion (notably, in the case of 3D growth, the measured data points would fall above these lines).[87] One should also mention at this point that prior to the present AFM study, this type of analysis by ARXPS was the only applied route to follow the multilayer growth of ILs on solid surfaces on the molecular scale.[87,102]

The formation of a two-dimensional wetting layer with a checkerboard arrangement of alternating anions and cations is very common for ILs on metal surfaces.[87] We propose that this structure is driven by the strong attractive interaction of cations and anions with their respective image charges in the metal.[85] This arrangement yields oppositely oriented dipoles (ion + image charge) with attractive lateral interactions within the wetting layer. On top of this wetting layer further growth then occurs in the form of oppositely oriented ion pair dipoles. This arrangement is schematically depicted in Figure 5. The situation is different from that observed, e.g., for the growth of the classical salt NaCl on Au(111), where already the initial growth occurs in bilayer islands.[109]

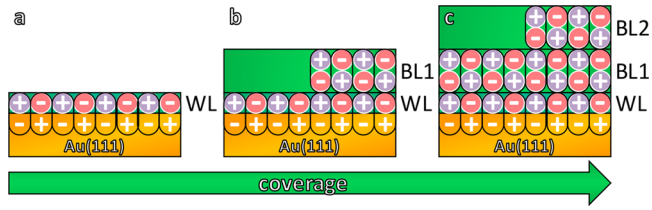

Figure 5. Schematic of the growth behavior of $[C_1C_1Im][Tf_2N]$ on Au(111). At low coverages, a wetting layer forms (a) with cations and anions arranged next to each other in a checkerboard fashion. The ions form oppositely oriented dipoles with the image charges in the substrate. In the multilayer range, the islands grow as bilayers, BL1 (b) and BL2 (c), of oppositely oriented ion pairs. The arrangement in the bilayers is similar to that in the striped phase of the wetting layer.[1] The wetting layer has only one-half of the height of the subsequent bilayers. Each layer is laterally stabilized by the attractive interactions of the oppositely oriented dipoles.

Overall, our observations concerning layering during the growth of ultrathin IL films on Au(111) are in quite good agreement with IL layering observed close to solid surfaces by force−distance AFM curves for macroscopic IL films or droplets under ambient pressure conditions. Depending on the systems under investigation, the first resolved layer was typically found either with a considerably lower thickness or with a thickness similar to the successive layers.[2,67−78] For comparison with $[C_1C_1Im][Tf_2N]$ studied here, we focus on the closely related systems $[C_2C_1Im][Tf_2N]$ on Au(111) and $[C_2C_1Im][Tf_2N]$ on Ag(111) investigated by Atkin et al. and Li et al., respectively.[67,76] For these two systems, the authors reported layer thicknesses of 0.65/0.75/0.65 nm and 0.77/~0.88/~0.88 nm for the first three resolvable layers. This is to be compared to the values of 0.37/0.69/0.72 nm obtained here. While the values for the second and third layer agree very well within the margin of error (note that we expect a slightly smaller value in our case due the methyl group in the cation instead of the one ethyl side chain), the value for the first resolved layer is different. A relatively simple explanation

https://dx.doi.org/10.1021/acs.langmuir.0c02596
Langmuir 2020, 36, 13670−13681

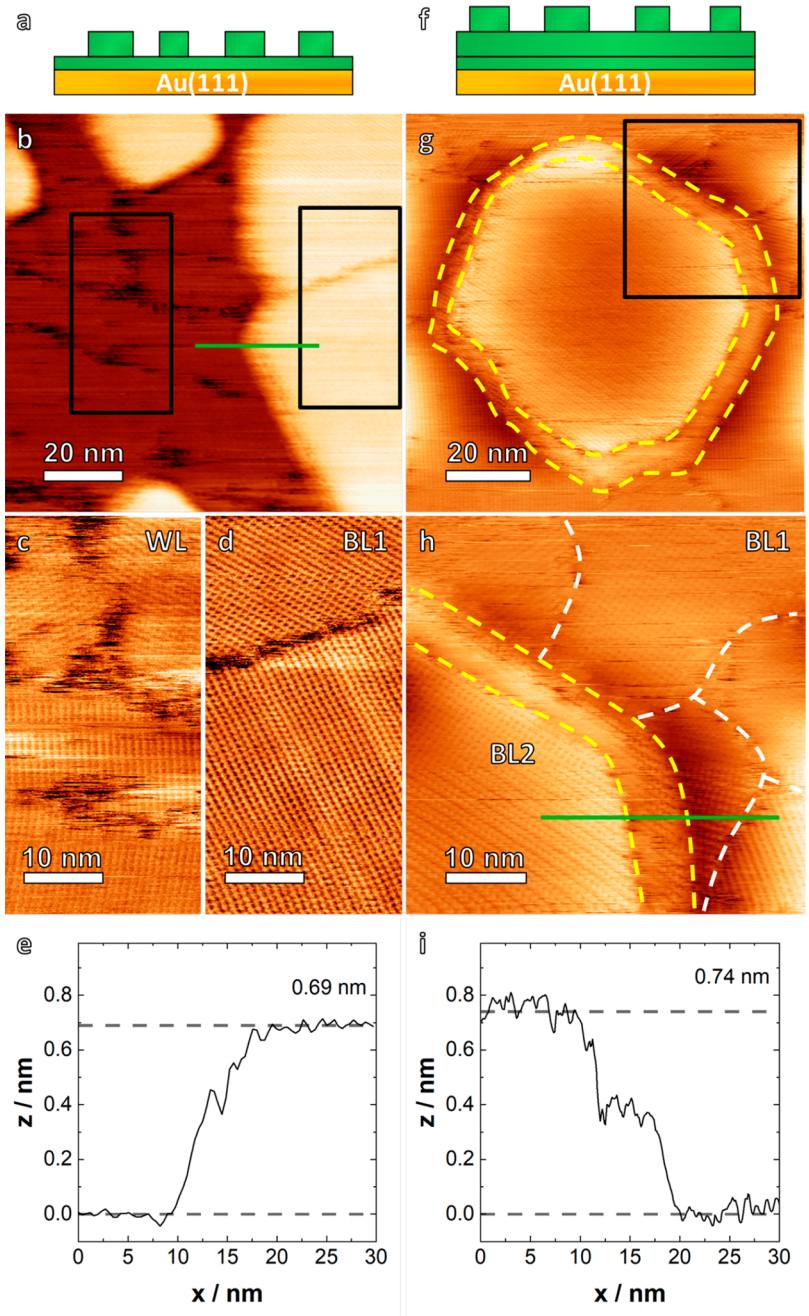

Figure 6. AFM images with molecular resolution of the islands in the multilayer range of $[C_1C_1Im][Tf_2N]$ on Au(111) after annealing to 250 K, measured at 110 K. (a–e) BL1 islands on top of the WL (2.00 WLE); (f–i) BL2 islands on top of the BL1 (4.00 WLE). In the enlarged images (areas indicated by black rectangles in the images above), the molecular structures of BL1 (d, h) and BL2 (h) are identified as striped phases, resembling the striped phase of the wetting layer (c) reported in a previous study.[1] The heights of BL1 and BL2, as deduced from the line profiles (e and i, respectively), agree with the average heights of 0.71 ± 0.05 nm deduced from Figure 2 within the margins of error. Notably, for BL2 at the edges of the islands (g) two steps with one-half the height are observed. Fourier transformations of the images and AFM parameters are provided in the SI.

would be that the wetting layer observed by us using UHV-AFM and XPS cannot be ruptured in the force–distance curves in ambient AFM due to its strong interaction with the Au(111) and Ag(111) substrates, and thus only the second/third/fourth layers are seen in the force–distance curves. Indeed, in their report on $[C_2C_1Im][FAP]$, $[C_4C_1Im][FAP]$, and $[C_6C_1Im][FAP]$ on Au(111) the group of Atkin reported thicknesses of 0.62/0.88/0.90 nm for $[C_2C_1Im][FAP]$ but stated that they could not rupture the interfacial layer.[71]

Next, we address the surface structure of the different layers. Figure 6 shows high-resolution images of the molecular arrangement of the WL, BL1, and BL2 for IL doses of 2 WLE (left; Figure 6a–e) and 4 WLE (right, Figure 6f–i). Each film was first annealed up to 250 K to form large islands; the subsequent measurements were performed at 110 K to obtain a better molecular resolution. The AFM image after a dose of 2.00 WLE, that is, a partly filled BL1 on top of the closed wetting layer, is shown in Figure 6b. The enlarged image of the wetting layer in Figure 6c shows different domains of the

https://dx.doi.org/10.1021/acs.langmuir.0c02596
Langmuir 2020, 36, 13670–13681

striped phase, which is one of the two low-temperature phases already reported by us for the wetting layer of $[C_1C_1Im][Tf_2N]$ on Au(111).[1] The enlarged image of BL1 in Figure 1d reveals a molecular arrangement which is, within the margin of error, identical to the striped phase in the wetting layer (Fourier transformations of selected areas are shown in Figure S3 in the SI). Notably, the structure of the wetting layer observed by AFM is assigned to the anions, while the cations are not visible.[1] The height profile across a step edge in Figure 6e yields a step height of 0. 69 ± 0.05 nm, in good agreement with Figure 2.

Figure 6 (right) shows the data for an IL dose of 4.00 WLE, which corresponds to a half-filled BL2 on top of a closed BL1 (Figure 6g). The surface structures of BL2 and BL1, which are resolved in the enlarged image in Figure 6h, are again equal to that of the striped phase observed for the wetting layer.[1] This similarity is also evident from the Fourier transformations of selected areas of the WL, BL1, and BL2 (see Figure S3 in the SI). Interestingly, at the edges of this BL2 island on BL1 in Figure 6h (right) and in particular in the height profile in Figure 6i, we observe steps of 0.37 ± 0.05 nm, that is, one-half the height of the bilayer step (0.71 ± 0.05 nm). This indicates that formation of BL2 on top of BL1 is strictly observed only within the islands but not at their edges. This behavior could be due to the lower coordination at the island edges.

SUMMARY AND CONCLUSIONS

We investigated the growth of the wetting layer and successive multilayers of $[C_1C_1Im][Tf_2N]$ on Au(111) by atomic force microscopy in ultrahigh vacuum. The IL films were deposited onto the surface at temperatures below 170 K. By monitoring the IL flux with a quartz crystal microbalance in situ during deposition we are able to precisely correlate the evaporated IL dose to the coverage obtained from AFM images. Through AFM measurements at 110, 200, 250, and 300 K, we followed the temperature-dependent ripening and structure of the deposited films. Initially, we observe the formation of a wetting layer with a thickness of ∼0.37 nm (as determined from XPS) with anions and cations arranged in a checkerboard structure. While this wetting layer can be imaged at 300 K, we were not able to obtain images of multilayers at this temperature due to unstable imaging conditions and slow multilayer desorption. At 250 K, however, we are able to follow the successive growth of IL multilayers in a bilayer-by-bilayer fashion (BL1 and BL2); these bilayers have double the height of the wetting layer. The growth behavior is independently determined from the fraction of the surface area covered with a particular IL layer as determined from the UHV AFM images and from AFM height profiles of the observed islands. Moreover, the height of the wetting layer and the overall layer-by-layer growth behavior is confirmed by angle-resolved X-ray photoelectron spectroscopy. The surface structure of the different layers could be resolved by high-resolution AFM at 110 K. The two bilayers BL1 and BL2 display a striped phase, which is one of the phases also seen for the wetting layer; for the wetting layer, the observed structure was assigned to the anions, while the cations were not visible.[1] Overall, our results concerning layering behavior and layer thickness are in agreement with ambient AFM studies in macroscopic films and droplets of similar ILs on Au(111) and Ag(111). The main differences are that with UHV-based AFM we clearly can determine the molecular structure of all layers (wetting layer, BL1 and BL2) and we do not face the problem that the first layer possibly is not resolved, because it cannot be ruptured in the force−distance measurements. Also, under the ultraclean conditions in ultrahigh vacuum, we expect no influence from contaminations like water.

EXPERIMENTAL SECTION

The atomic force microscopy (AFM) experiments were carried out in a Scienta Omicron two-chamber UHV system with a base pressure of $<1 \times 10^{-10}$ mbar. The variable-temperature AFM/STM microscope is a Scienta Omicron VT-AFM-Q+-XA. The AFM images were recorded in noncontact mode, and the given frequency shift refers to the respective cantilever resonance frequency, typically around 300 kHz. The applied frequency window of the cantilever, Δf, typically ranged from −150 to −500 Hz. The images were processed with WSxM[110] software, and moderate filtering (Gaussian smooth, background subtraction) was applied for noise reduction.

$[C_1C_1Im][Tf_2N]$ was synthesized under ultrapure conditions according to previous publications.[53] Notably, the anion $[Tf_2N]^-$ is also known as $[NTf_2]^-$ [14,27,45] or $[TFSA]^-$,[24,30] and the cation $[C_1C_1Im]^+$ is also known as $[MMIm]^+$[111] in the literature. The Au(111) single crystal (MaTecK) was cleaned via Ar^+ ion sputtering and annealing at 900 K. The IL was deposited with an effusion cell, developed in our group explicitly for IL deposition,[103] at cell temperatures between 373 and 383 K. The flux was checked with a quartz crystal microbalance (QCM), calibrated by determining the ratio of IL-covered and uncovered area on the single crystal by AFM. The covered area was measured by cutting out images on a single terrace, applying a background subtraction, and "flooding" the images at a threshold of 50% the height of the IL islands in WSxM (SI Figure S4).[110] The error bars were estimated by the same procedure with a threshold of 75%. For very small structure diameters, the edges of the structure are often broadened by about one-half of the diameter of the scanning tip apex. To minimize the influence of this effect, only images were used where the diameter of the islands was about 50−100 nm and therefore significantly larger than the tip.

The UHV system for angle-resolved X-ray photoelectron spectroscopy (ARXPS) was described previously in more detail.[112] We acquired ARXP spectra with a nonmonochromated Al Kα X-ray source (SPECS XR 50, 1486.6 eV, 240 W) and a hemispherical electron analyzer (VG SCIENTA R3000). We measured at a pass energy of 100 eV, resulting in an overall energy resolution of ∼0.9 eV. Peak fitting and background subtraction was done using CasaXPS V2.3.1Dev6. For analysis of the Au 4f intensity, we subtracted a Shirley background.[113]

We studied the coverage and growth of the IL films by measuring the attenuation of the Au 4f signal of the Au(111) crystal as a function of IL film thickness at emission angles of $\vartheta = 0°$ and 80° relative to the surface normal. For homogeneous two-dimensional growth, the Au 4f signals decrease exponentially from I_0 (clean surface) to I_d (when the surface is covered with a film of thickness d) according to

$$\frac{I_d}{I_0} = e^{-d/\lambda \cdot \cos \vartheta} \tag{1}$$

with $\lambda = 3.0$ nm for Au 4f electrons (with a kinetic energy of about 1.4 keV) in IL films.[87,102] For 2D layer-by-layer growth, where each layer is completed before a new layer starts to grow on top, the substrate signals decrease in a section-wise linear fashion for each layer.[114]

The film morphology was investigated by first determining the film thickness d from the I_d/I_0 ratio at $\vartheta = 0°$ using eq 1. With this thickness, we then calculated the 80° value expected for 2D growth. Agreement between the experimental and the calculated data for 80° indicates 2D growth. If $I_d/I_0(80°)$ lies above the calculated curve, it indicates a 3D morphology of the IL film.[87]

ASSOCIATED CONTENT

Supporting Information

The Supporting Information is available free of charge at https://pubs.acs.org/doi/10.1021/acs.langmuir.0c02596.

https://dx.doi.org/10.1021/acs.langmuir.0c02596
Langmuir 2020, 36, 13670−13681

Information on the calibration of the evaporation rate with the quartz microbalance; instability of the AFM in the multilayer range above 280 K; Fourier transformations of the AFM images of the wetting layer and bilayers BL1 and BL2; coverage determination from AFM images; detailed account of the preparation conditions of all presented AFM images (PDF)

AUTHOR INFORMATION

Corresponding Author

Hans-Peter Steinrück − *Lehrstuhl für Physikalische Chemie II, Universität Erlangen-Nürnberg, 91058 Erlangen, Germany;* orcid.org/0000-0003-1347-8962; Email: hans-peter.steinrueck@fau.de

Authors

Manuel Meusel − *Lehrstuhl für Physikalische Chemie II, Universität Erlangen-Nürnberg, 91058 Erlangen, Germany*

Matthias Lexow − *Lehrstuhl für Physikalische Chemie II, Universität Erlangen-Nürnberg, 91058 Erlangen, Germany;* orcid.org/0000-0002-1441-2909

Afra Gezmis − *Lehrstuhl für Physikalische Chemie II, Universität Erlangen-Nürnberg, 91058 Erlangen, Germany*

Andreas Bayer − *Lehrstuhl für Physikalische Chemie II, Universität Erlangen-Nürnberg, 91058 Erlangen, Germany*

Florian Maier − *Lehrstuhl für Physikalische Chemie II, Universität Erlangen-Nürnberg, 91058 Erlangen, Germany;* orcid.org/0000-0001-9725-8961

Complete contact information is available at: https://pubs.acs.org/10.1021/acs.langmuir.0c02596

Notes

The authors declare no competing financial interest.

ACKNOWLEDGMENTS

We thank Nicola Taccardi for the synthesis of $[C_1C_1Im][Tf_2N]$. M.M., M.L., and H.-P.S. thank the European Research Council (ERC) under the European Union's Horizon 2020 research and innovation programme for financial support in the context of the Advanced Investigator Grant "ILID" to H.-P.S. (Grant Agreement No. 693398-ILID).

REFERENCES

(1) Meusel, M.; Lexow, M.; Gezmis, A.; Schotz, S.; Wagner, M.; Bayer, A.; Maier, F.; Steinrück, H. P. Atomic Force and Scanning Tunneling Microscopy of Ordered Ionic Liquid Wetting Layers from 110 K up to Room Temperature. *ACS Nano* **2020**, *14*, 9000−9010.

(2) Hayes, R.; Warr, G. G.; Atkin, R. Structure and nanostructure in ionic liquids. *Chem. Rev.* **2015**, *115*, 6357−426.

(3) Lovelock, K. R.; Villar-Garcia, I. J.; Maier, F.; Steinrück, H. P.; Licence, P. Photoelectron spectroscopy of ionic liquid-based interfaces. *Chem. Rev.* **2010**, *110*, 5158−90.

(4) Steinrück, H. P. Recent developments in the study of ionic liquid interfaces using X-ray photoelectron spectroscopy and potential future directions. *Phys. Chem. Chem. Phys.* **2012**, *14*, 5010−29.

(5) Heym, F.; Etzold, B. J. M.; Kern, C.; Jess, A. Analysis of evaporation and thermal decomposition of ionic liquids by thermogravimetrical analysis at ambient pressure and high vacuum. *Green Chem.* **2011**, *13*, 1453−1466.

(6) Zaitsau, D. H.; Yermalayeu, A. V.; Schubert, T. J. S.; Verevkin, S. P. Alkyl-imidazolium tetrafluoroborates: Vapor pressure, thermodynamics of vaporization, and enthalpies of formation. *J. Mol. Liq.* **2017**, *242*, 951−957.

(7) Zaitsau, D. H.; Yermalayeu, A. V.; Emel'yanenko, V. N.; Butler, S.; Schubert, T.; Verevkin, S. P. Thermodynamics of Imidazolium-Based Ionic Liquids Containing PF6 Anions. *J. Phys. Chem. B* **2016**, *120*, 7949−57.

(8) Zaitsau, D. H.; Yermalayeu, A. V.; Emel'yanenko, V. N.; Verevkin, S. P. Thermodynamics of Imidazolium-Based Ionic Liquids Containing the Trifluoromethanesulfonate Anion. *Chem. Eng. Technol.* **2018**, *41*, 1604−1612.

(9) Zaitsau, D. H.; Kabo, G. J.; Strechan, A. A.; Paulechka, Y. U.; Tschersich, A.; Verevkin, S. P.; Heintz, A. Experimental vapor pressures of 1-alkyl-3-methylimidazolium bis-(trifluoromethylsulfonyl)imides and a correlation scheme for estimation of vaporization enthalpies of ionic liquids. *J. Phys. Chem. A* **2006**, *110*, 7303−6.

(10) Plechkova, N. V.; Seddon, K. R. Applications of ionic liquids in the chemical industry. *Chem. Soc. Rev.* **2008**, *37*, 123−50.

(11) Seddon, K. R. Ionic liquids: a taste of the future. *Nat. Mater.* **2003**, *2*, 363−5.

(12) Zhou, F.; Liang, Y.; Liu, W. Ionic liquid lubricants: designed chemistry for engineering applications. *Chem. Soc. Rev.* **2009**, *38*, 2590−9.

(13) Cooper, P. K.; Wear, C. J.; Li, H.; Atkin, R. Ionic Liquid Lubrication of Stainless Steel: Friction is Inversely Correlated with Interfacial Liquid Nanostructure. *ACS Sustainable Chem. Eng.* **2017**, *5*, 11737−11743.

(14) Cooper, P. K.; Staddon, J.; Zhang, S.; Aman, Z. M.; Atkin, R.; Li, H. Nano- and Macroscale Study of the Lubrication of Titania Using Pure and Diluted Ionic Liquids. *Front. Chem.* **2019**, *7*, 287.

(15) Armstrong, D. W.; He, L.; Liu, Y. S. Examination of ionic liquids and their interaction with molecules, when used as stationary phases in gas chromatography. *Anal. Chem.* **1999**, *71*, 3873−6.

(16) Anderson, J. L.; Armstrong, D. W. Immobilized ionic liquids as high-selectivity/high-temperature/high-stability gas chromatography stationary phases. *Anal. Chem.* **2005**, *77*, 6453−62.

(17) Joshi, M. D.; Anderson, J. L. Recent advances of ionic liquids in separation science and mass spectrometry. *RSC Adv.* **2012**, *2*, 5470−5484.

(18) Ho, T. D.; Zhang, C.; Hantao, L. W.; Anderson, J. L. Ionic liquids in analytical chemistry: fundamentals, advances, and perspectives. *Anal. Chem.* **2014**, *86*, 262−85.

(19) Odugbesi, G. A.; Nan, H.; Soltani, M.; Davis, J. H., Jr.; Anderson, J. L. Ultra-high thermal stability perarylated ionic liquids as gas chromatographic stationary phases for the selective separation of polyaromatic hydrocarbons and polychlorinated biphenyls. *J. Chromatogr, A* **2019**, *1604*, 460466.

(20) Goossens, K.; Lava, K.; Bielawski, C. W.; Binnemans, K. Ionic Liquid Crystals: Versatile Materials. *Chem. Rev.* **2016**, *116*, 4643−807.

(21) Binnemans, K. Ionic liquid crystals. *Chem. Rev.* **2005**, *105*, 4148−204.

(22) Johnston, M.; Lee, J. J.; Chottiner, G. S.; Miller, B.; Tsuda, T.; Hussey, C. L.; Scherson, D. A. Electrochemistry in ultrahigh vacuum: underpotential deposition of Al on polycrystalline W and Au from room temperature AlCl(3)/1-ethyl-3-methylimidazolium chloride melts. *J. Phys. Chem. B* **2005**, *109*, 11296−300.

(23) Hapiot, P.; Lagrost, C. Electrochemical reactivity in room-temperature ionic liquids. *Chem. Rev.* **2008**, *108*, 2238−64.

(24) Endres, F.; Hofft, O.; Borisenko, N.; Gasparotto, L. H.; Prowald, A.; Al-Salman, R.; Carstens, T.; Atkin, R.; Bund, A.; Zein El Abedin, S. Do solvation layers of ionic liquids influence electrochemical reactions? *Phys. Chem. Chem. Phys.* **2010**, *12*, 1724−32.

(25) Armand, M.; Endres, F.; MacFarlane, D. R.; Ohno, H.; Scrosati, B. Ionic-liquid materials for the electrochemical challenges of the future. *Nat. Mater.* **2009**, *8*, 621−629.

(26) Weingarth, D.; Foelske-Schmitz, A.; Wokaun, A.; Kotz, R. In situ electrochemical XPS study of the Pt/[EMIM][BF4] system. *Electrochem. Commun.* **2011**, *13*, 619−622.

(27) Reyna-González, J. M.; Reyes-López, J. C.; Aguilar-Martínez, M. Silver and silver-copper electrodeposition from a pyridinium-based ionic liquid. *Electrochim. Acta* **2013**, *94*, 344−352.

(28) Liu, Z.; Cui, T.; Lu, T.; Shapouri Ghazvini, M.; Endres, F. Anion Effects on the Solid/Ionic Liquid Interface and the Electrodeposition of Zinc. *J. Phys. Chem. C* **2016**, *120*, 20224−20231.
(29) Iwahashi, T.; Miwa, Y.; Zhou, W.; Sakai, Y.; Yamagata, M.; Ishikawa, M.; Kim, D.; Ouchi, Y. IV-SFG studies on the effect of Li+ in extending the electrochemical window at the Pt |[C2mim][FSA] interface. *Electrochem. Commun.* **2016**, *72*, 54−58.
(30) Hoffmann, V.; Pulletikurthi, G.; Carstens, T.; Lahiri, A.; Borodin, A.; Schammer, M.; Horstmann, B.; Latz, A.; Endres, F. Influence of a silver salt on the nanostructure of a Au(111)/ionic liquid interface: an atomic force microscopy study and theoretical concepts. *Phys. Chem. Chem. Phys.* **2018**, *20*, 4760−4771.
(31) Welton, T. Room-Temperature Ionic Liquids. Solvents for Synthesis and Catalysis. *Chem. Rev.* **1999**, *99*, 2071−2084.
(32) Mehnert, C. P.; Mozeleski, E. J.; Cook, R. A. Supported ionic liquid catalysis investigated for hydrogenation reactions. *Chem. Commun. (Cambridge, U. K.)* **2002**, 3010−1.
(33) Huang, J.; Jiang, T.; Gao, H.; Han, B.; Liu, Z.; Wu, W.; Chang, Y.; Zhao, G. Pd nanoparticles immobilized on molecular sieves by ionic liquids: heterogeneous catalysts for solvent-free hydrogenation. *Angew. Chem., Int. Ed.* **2004**, *43*, 1397−9.
(34) Breitenlechner, S.; Fleck, M.; Muller, T. E.; Suppan, A. Solid catalysts on the basis of supported ionic liquids and their use in hydroamination reactions. *J. Mol. Catal. A: Chem.* **2004**, *214*, 175−179.
(35) Riisager, A.; Fehrmann, R.; Haumann, M.; Gorle, B. S. K.; Wasserscheid, P. Stability and kinetic studies of supported ionic liquid phase catalysts for hydroformylation of propene. *Ind. Eng. Chem. Res.* **2005**, *44*, 9853−9859.
(36) Riisager, A.; Fehrmann, R.; Flicker, S.; van Hal, R.; Haumann, M.; Wasserscheid, P. Very stable and highly regioselective supported ionic-liquid-phase (SILP) catalysis: continuous-flow fixed-bed hydroformylation of propene. *Angew. Chem., Int. Ed.* **2005**, *44*, 815−9.
(37) Mehnert, C. P.; Cook, R. A.; Dispenziere, N. C.; Afeworki, M. Supported ionic liquid catalysis–a new concept for homogeneous hydroformylation catalysis. *J. Am. Chem. Soc.* **2002**, *124*, 12932−3.
(38) Riisager, A.; Fehrmann, R.; Haumann, M.; Wasserscheid, P. Supported ionic liquids: versatile reaction and separation media. *Top. Catal.* **2006**, *40*, 91−102.
(39) Kernchen, U.; Etzold, B.; Korth, W.; Jess, A. Solid Catalyst with Ionic Liquid Layer (SCILL) - A New Concept to Improve Selectivity Illustrated by Hydrogenation of Cyclooctadiene. *Chem. Eng. Technol.* **2007**, *30*, 985−994.
(40) Wasserscheid, P.; Keim, W. Ionic Liquids—New "Solutions" for Transition Metal Catalysis. *Angew. Chem., Int. Ed.* **2000**, *39*, 3772−3789.
(41) Wasserscheid, P.; Welton, T. *Ionic liquids in synthesis*; John Wiley & Sons:, 2008.
(42) Steinrück, H.-P.; Wasserscheid, P. Ionic Liquids in Catalysis. *Catal. Lett.* **2015**, *145*, 380−397.
(43) Gu, Y.; Ogawa, C.; Kobayashi, J.; Mori, Y.; Kobayashi, S. A heterogeneous silica-supported scandium/ionic liquid catalyst system for organic reactions in water. *Angew. Chem., Int. Ed.* **2006**, *45*, 7217−20.
(44) Castner, E. W.; Wishart, J. F. Spotlight on ionic liquids. *J. Chem. Phys.* **2010**, *132*, 120901.
(45) Heinze, M. T.; Zill, J. C.; Matysik, J.; Einicke, W. D.; Glaser, R.; Stark, A. Solid-ionic liquid interfaces: pore filling revisited. *Phys. Chem. Chem. Phys.* **2014**, *16*, 24359−72.
(46) Steinrück, H. P.; Libuda, J.; Wasserscheid, P.; Cremer, T.; Kolbeck, C.; Laurin, M.; Maier, F.; Sobota, M.; Schulz, P. S.; Stark, M. Surface science and model catalysis with ionic liquid-modified materials. *Adv. Mater.* **2011**, *23*, 2571−87.
(47) Schernich, S.; Laurin, M.; Lykhach, Y.; Tsud, N.; Sobota, M.; Skala, T.; Prince, K. C.; Taccardi, N.; Wagner, V.; Steinrück, H. P.; Matolin, V.; Wasserscheid, P.; Libuda, J. Interactions of imidazolium-based ionic liquids with oxide surfaces controlled by alkyl chain functionalization. *ChemPhysChem* **2013**, *14*, 3673−7.
(48) Schernich, S.; Laurin, M.; Lykhach, Y.; Steinrück, H. P.; Tsud, N.; Skala, T.; Prince, K. C.; Taccardi, N.; Matolin, V.; Wasserscheid, P.; Libuda, J. Functionalization of Oxide Surfaces through Reaction with 1,3-Dialkylimidazolium Ionic Liquids. *J. Phys. Chem. Lett.* **2013**, *4*, 30−5.
(49) Steinrück, H. P. Surface science goes liquid! *Surf. Sci.* **2010**, *604*, 481−484.
(50) Lockett, V.; Sedev, R.; Harmer, S.; Ralston, J.; Horne, M.; Rodopoulos, T. Orientation and mutual location of ions at the surface of ionic liquids. *Phys. Chem. Chem. Phys.* **2010**, *12*, 13816−27.
(51) Lovelock, K. R. Influence of the ionic liquid/gas surface on ionic liquid chemistry. *Phys. Chem. Chem. Phys.* **2012**, *14*, 5071−89.
(52) Kolbeck, C.; Deyko, A.; Matsuda, T.; Kohler, F. T.; Wasserscheid, P.; Maier, F.; Steinrück, H. P. Temperature-dependent surface-enrichment effects of imidazolium-based ionic liquids. *ChemPhysChem* **2013**, *14*, 3726−30.
(53) Lovelock, K. R.; Kolbeck, C.; Cremer, T.; Paape, N.; Schulz, P. S.; Wasserscheid, P.; Maier, F.; Steinrück, H. P. Influence of different substituents on the surface composition of ionic liquids studied using ARXPS. *J. Phys. Chem. B* **2009**, *113*, 2854−64.
(54) Sobota, M.; Nikiforidis, I.; Hieringer, W.; Paape, N.; Happel, M.; Steinrück, H. P.; Gorling, A.; Wasserscheid, P.; Laurin, M.; Libuda, J. Toward ionic-liquid-based model catalysis: growth, orientation, conformation, and interaction mechanism of the [Tf2N]- anion in [BMIM][Tf2N] thin films on a well-ordered alumina surface. *Langmuir* **2010**, *26*, 7199−207.
(55) Jeon, Y.; Sung, J.; Bu, W.; Vaknin, D.; Ouchi, Y.; Kim, D. Interfacial Restructuring of Ionic Liquids Determined by Sum-Frequency Generation Spectroscopy and X-Ray Reflectivity. *J. Phys. Chem. C* **2008**, *112*, 19649−19654.
(56) Santos, C. S.; Baldelli, S. Gas-liquid interface of room-temperature ionic liquids. *Chem. Soc. Rev.* **2010**, *39*, 2136−45.
(57) Sloutskin, E.; Ocko, B. M.; Tamam, L.; Kuzmenko, I.; Gog, T.; Deutsch, M. Surface layering in ionic liquids: an X-ray reflectivity study. *J. Am. Chem. Soc.* **2005**, *127*, 7796−804.
(58) Yano, Y. F.; Yamada, H. Surface structure of a neat ionic liquid investigated by grazing-incidence x-ray diffraction. *Anal. Sci.* **2008**, *24*, 1269−71.
(59) Pajkossy, T.; Kolb, D. M. The interfacial capacitance of Au(100) in an ionic liquid, 1-butyl-3-methyl-imidazolium hexafluorophosphate. *Electrochem. Commun.* **2011**, *13*, 284−286.
(60) Greco, F.; Shin, S.; Williams, F. J.; Heller, B. S. J.; Maier, F.; Steinrück, H. P. Potential Screening at Electrode/Ionic Liquid Interfaces from In Situ X-ray Photoelectron Spectroscopy. *ChemistryOpen* **2019**, *8*, 1365−1368.
(61) Zheng, J. P.; Goonetilleke, P. C.; Pettit, C. M.; Roy, D. Probing the electrochemical double layer of an ionic liquid using voltammetry and impedance spectroscopy: a comparative study of carbon nanotube and glassy carbon electrodes in [EMIM](+)[EtSO(4)](−). *Talanta* **2010**, *81*, 1045−55.
(62) Silva, F.; Gomes, C.; Figueiredo, M.; Costa, R.; Martins, A.; Pereira, C. M. The electrical double layer at the [BMIM][PF6] ionic liquid/electrode interface - Effect of temperature on the differential capacitance. *J. Electroanal. Chem.* **2008**, *622*, 153−160.
(63) Zheng, J.; Moganty, S. S.; Goonetilleke, P. C.; Baltus, R. E.; Roy, D. A Comparative Study of the Electrochemical Characteristics of [Emim+][BF4-] and [Bmim+][BF4-] Ionic Liquids at the Surfaces of Carbon Nanotube and Glassy Carbon Electrodes. *J. Phys. Chem. C* **2011**, *115*, 7527−7537.
(64) Islam, M. M.; Alam, M. T.; Ohsaka, T. Electrical Double-Layer Structure in Ionic Liquids: A Corroboration of the Theoretical Model by Experimental Results. *J. Phys. Chem. C* **2008**, *112*, 16568−16574.
(65) Yokota, Y.; Harada, T.; Fukui, K. Direct observation of layered structures at ionic liquid/solid interfaces by using frequency-modulation atomic force microscopy. *Chem. Commun. (Cambridge, U. K.)* **2010**, *46*, 8627−9.
(66) Yokota, Y.; Hara, H.; Harada, T.; Imanishi, A.; Uemura, T.; Takeya, J.; Fukui, K. Structural investigation of ionic liquid/rubrene

https://dx.doi.org/10.1021/acs.langmuir.0c02596
Langmuir 2020, 36, 13670−13681

single crystal interfaces by using frequency-modulation atomic force microscopy. *Chem. Commun. (Cambridge, U. K.)* **2013**, *49*, 10596−8.
(67) Li, M.-G.; Chen, L.; Zhong, Y.-X.; Chen, Z.-B.; Yan, J.-W.; Mao, B.-W. The electrochemical interface of Ag(111) in 1-ethyl-3-methylimidazolium bis(trifluoromethylsulfonyl)imide ionic liquid—A combined in-situ scanning probe microscopy and impedance study. *Electrochim. Acta* **2016**, *197*, 282−289.
(68) Cheng, H. W.; Dienemann, J. N.; Stock, P.; Merola, C.; Chen, Y. J.; Valtiner, M. The Effect of Water and Confinement on Self-Assembly of Imidazolium Based Ionic Liquids at Mica Interfaces. *Sci. Rep.* **2016**, *6*, 30058.
(69) Cheng, H.-W.; Stock, P.; Moeremans, B.; Baimpos, T.; Banquy, X.; Renner, F. U.; Valtiner, M. Characterizing the Influence of Water on Charging and Layering at Electrified Ionic-Liquid/Solid Interfaces. *Adv. Mater. Interfaces* **2015**, *2*, 1500159.
(70) McIntosh, E. M.; Ellis, J.; Jardine, A. P.; Licence, P.; Jones, R. G.; Allison, W. Probing liquid behaviour by helium atom scattering: surface structure and phase transitions of an ionic liquid on Au(111). *Chem. Sci.* **2014**, *5*, 667−676.
(71) Li, H.; Endres, F.; Atkin, R. Effect of alkyl chain length and anion species on the interfacial nanostructure of ionic liquids at the Au(111)-ionic liquid interface as a function of potential. *Phys. Chem. Chem. Phys.* **2013**, *15*, 14624−33.
(72) Li, H.; Wood, R. J.; Endres, F.; Atkin, R. Influence of alkyl chain length and anion species on ionic liquid structure at the graphite interface as a function of applied potential. *J. Phys.: Condens. Matter* **2014**, *26*, 284115.
(73) Zhong, Y. X.; Yan, J. W.; Li, M. G.; Zhang, X.; He, D. W.; Mao, B. W. Resolving fine structures of the electric double layer of electrochemical interfaces in ionic liquids with an AFM tip modification strategy. *J. Am. Chem. Soc.* **2014**, *136*, 14682−5.
(74) Zhong, Y. X.; Yan, J. W.; Li, M. G.; Chen, L.; Mao, B. W. The Electric Double Layer in an Ionic Liquid Incorporated with Water Molecules: Atomic Force Microscopy Force Curve Study. *ChemElectroChem* **2016**, *3*, 2221−2226.
(75) Zhang, X.; Zhong, Y. X.; Yan, J. W.; Su, Y. Z.; Zhang, M.; Mao, B. W. Probing double layer structures of Au (111)-BMIPF6 ionic liquid interfaces from potential-dependent AFM force curves. *Chem. Commun. (Cambridge, U. K.)* **2012**, *48*, 582−4.
(76) Atkin, R.; El Abedin, S. Z.; Hayes, R.; Gasparotto, L. H. S.; Borisenko, N.; Endres, F. AFM and STM Studies on the Surface Interaction of [BMP]TFSA and (EMIm]TFSA Ionic Liquids with Au(111). *J. Phys. Chem. C* **2009**, *113*, 13266−13272.
(77) Hayes, R.; Borisenko, N.; Tam, M. K.; Howlett, P. C.; Endres, F.; Atkin, R. Double Layer Structure of Ionic Liquids at the Au(111) Electrode Interface: An Atomic Force Microscopy Investigation. *J. Phys. Chem. C* **2011**, *115*, 6855−6863.
(78) Endres, F.; Borisenko, N.; El Abedin, S. Z.; Hayes, R.; Atkin, R. The interface ionic liquid(s)/electrode(s): in situ STM and AFM measurements. *Faraday Discuss.* **2012**, *154*, 221−233.
(79) Atkin, R.; Warr, G. G. Structure in Confined Room-Temperature Ionic Liquids. *J. Phys. Chem. C* **2007**, *111*, 5162−5168.
(80) Fukui, K.; Yokota, Y.; Imanishi, A. Local analyses of ionic liquid/solid interfaces by frequency modulation atomic force microscopy and photoemission spectroscopy. *Chem. Rec* **2014**, *14*, 964−73.
(81) Page, A. J.; Elbourne, A.; Stefanovic, R.; Addicoat, M. A.; Warr, G. G.; Voitchovsky, K.; Atkin, R. 3-Dimensional atomic scale structure of the ionic liquid-graphite interface elucidated by AM-AFM and quantum chemical simulations. *Nanoscale* **2014**, *6*, 8100−6.
(82) Klaver, T. P. C.; Luppi, M.; Sluiter, M. H. F.; Kroon, M. C.; Thijsse, B. J. DFT Study of 1,3-Dimethylimidazolium Tetrafluoroborate on Al and Cu(111) Surfaces. *J. Phys. Chem. C* **2011**, *115*, 14718−14730.
(83) Jha, K. C.; Liu, H.; Bockstaller, M. R.; Heinz, H. Facet Recognition and Molecular Ordering of Ionic Liquids on Metal Surfaces. *J. Phys. Chem. C* **2013**, *117*, 25969−25981.
(84) Borghi, F.; Podesta, A. Ionic liquids under nanoscale confinement. *Adv. Phys: X* **2020**, *5*, 1736949.
(85) Ntim, S.; Sulpizi, M. Role of image charges in ionic liquid confined between metallic interfaces. *Phys. Chem. Chem. Phys.* **2020**, *22*, 10786−10791.
(86) Buraschi, M.; Sansotta, S.; Zahn, D. Polarization Effects in Dynamic Interfaces of Platinum Electrodes and Ionic Liquid Phases: A Molecular Dynamics Study. *J. Phys. Chem. C* **2020**, *124*, 2002−2007.
(87) Lexow, M.; Maier, F.; Steinrück, H.-P. Ultrathin ionic liquid films on metal surfaces: adsorption, growth, stability and exchange phenomena. *Adv. Phys: X* **2020**, *5*, 1761266.
(88) Cremer, T.; Killian, M.; Gottfried, J. M.; Paape, N.; Wasserscheid, P.; Maier, F.; Steinrück, H. P. Physical vapor deposition of [EMIM][Tf2N]: a new approach to the modification of surface properties with ultrathin ionic liquid films. *ChemPhysChem* **2008**, *9*, 2185−90.
(89) Souda, R. Glass-liquid transition, crystallization, and melting of a room temperature ionic liquid: thin films of 1-ethyl-3-methylimidazolium bis[trifluoromethanesulfonyl]imide studied with TOF-SIMS. *J. Phys. Chem. B* **2008**, *112*, 15349−54.
(90) Cui, T.; Lahiri, A.; Carstens, T.; Borisenko, N.; Pulletikurthi, G.; Kuhl, C.; Endres, F. Influence of Water on the Electrified Ionic Liquid/Solid Interface: A Direct Observation of the Transition from a Multilayered Structure to a Double-Layer Structure. *J. Phys. Chem. C* **2016**, *120*, 9341−9349.
(91) Broderick, A.; Newberg, J. T. Water at Ionic Liquid Interfaces. In *Ionic Liquids: Current State and Future Directions*; Shiflett, M. B., Scurto, A. M., Eds.; ACS Symposium Series 1250; American Chemical Society, 2017; pp 227−249.
(92) Gong, X.; Wang, B.; Li, L. Spreading of Nanodroplets of Ionic Liquids on the Mica Surface. *ACS Omega* **2018**, *3*, 16398−16402.
(93) Foulston, R.; Gangopadhyay, S.; Chiutu, C.; Moriarty, P.; Jones, R. G. Mono- and multi-layer adsorption of an ionic liquid on Au(110). *Phys. Chem. Chem. Phys.* **2012**, *14*, 6054−66.
(94) Uhl, B.; Buchner, F.; Gabler, S.; Bozorgchenani, M.; Jurgen Behm, R. Adsorption and reaction of sub-monolayer films of an ionic liquid on Cu(111). *Chem. Commun. (Cambridge, U. K.)* **2014**, *50*, 8601−4.
(95) Uhl, B.; Buchner, F.; Alwast, D.; Wagner, N.; Behm, R. J. Adsorption of the ionic liquid [BMP][TFSA] on Au(111) and Ag(111): substrate effects on the structure formation investigated by STM. *Beilstein J. Nanotechnol.* **2013**, *4*, 903−918.
(96) Uhl, B.; Cremer, T.; Roos, M.; Maier, F.; Steinrück, H. P.; Behm, R. J. At the ionic liquid|metal interface: structure formation and temperature dependent behavior of an ionic liquid adlayer on Au(111). *Phys. Chem. Chem. Phys.* **2013**, *15*, 17295−302.
(97) Waldmann, T.; Huang, H. H.; Hoster, H. E.; Hofft, O.; Endres, F.; Behm, R. J. Imaging an ionic liquid adlayer by scanning tunneling microscopy at the solid|vacuum interface. *ChemPhysChem* **2011**, *12*, 2565−7.
(98) Buchner, F.; Forster-Tonigold, K.; Bozorgchenani, M.; Gross, A.; Behm, R. J. Interaction of a Self-Assembled Ionic Liquid Layer with Graphite(0001): A Combined Experimental and Theoretical Study. *J. Phys. Chem. Lett.* **2016**, *7*, 226−33.
(99) Uhl, B.; Huang, H.; Alwast, D.; Buchner, F.; Behm, R. J. Interaction of ionic liquids with noble metal surfaces: structure formation and stability of [OMIM][TFSA] and [EMIM][TFSA] on Au(111) and Ag(111). *Phys. Chem. Chem. Phys.* **2015**, *17*, 23816−32.
(100) Uhl, B.; Hekmatfar, M.; Buchner, F.; Behm, R. J. Interaction of the ionic liquid [BMP][TFSA] with rutile TiO2(110) and coadsorbed lithium. *Phys. Chem. Chem. Phys.* **2016**, *18*, 6618−36.
(101) Buchner, F.; Forster-Tonigold, K.; Uhl, B.; Alwast, D.; Wagner, N.; Farkhondeh, H.; Gross, A.; Behm, R. J. Toward the microscopic identification of anions and cations at the ionic liquid|Ag(111) interface: a combined experimental and theoretical investigation. *ACS Nano* **2013**, *7*, 7773−84.
(102) Cremer, T.; Stark, M.; Deyko, A.; Steinrück, H. P.; Maier, F. Liquid/solid interface of ultrathin ionic liquid films: [C1C1Im]-[Tf2N] and [C8C1Im][Tf2N] on Au(111). *Langmuir* **2011**, *27*, 3662−71.

https://dx.doi.org/10.1021/acs.langmuir.0c02596
Langmuir 2020, 36, 13670−13681

(103) Lexow, M.; Heller, B. S. J.; Maier, F.; Steinrück, H. P. Anion Exchange at the Liquid/Solid Interface of Ultrathin Ionic Liquid Films on Ag(111). *ChemPhysChem* **2018**, *19*, 2978−2984.
(104) Winkler, A.; Tumbek, L. Nucleation of Organic Molecules via a Hot Precursor State: Pentacene on Amorphous Mica. *J. Phys. Chem. Lett.* **2013**, *4*, 4080−4084.
(105) Venables, J. A. Atomic processes in crystal growth. *Surf. Sci.* **1994**, *299−300*, 798−817.
(106) Zhang, Z.; Lagally, M. G. Atomistic Processes in the Early Stages of Thin-Film Growth. *Science* **1997**, *276*, 377−83.
(107) Rojas, G.; Chen, X.; Kunkel, D.; Bode, M.; Enders, A. Temperature dependence of metal-organic heteroepitaxy. *Langmuir* **2011**, *27*, 14267−71.
(108) Kolbeck, C.; Cremer, T.; Lovelock, K. R.; Paape, N.; Schulz, P. S.; Wasserscheid, P.; Maier, F.; Steinrück, H. P. Influence of different anions on the surface composition of ionic liquids studied using ARXPS. *J. Phys. Chem. B* **2009**, *113*, 8682−8.
(109) Lauwaet, K.; Schouteden, K.; Janssens, E.; Van Haesendonck, C.; Lievens, P. Dependence of the NaCl/Au(111) interface state on the thickness of the NaCl layer. *J. Phys.: Condens. Matter* **2012**, *24*, 475507.
(110) Horcas, I.; Fernandez, R.; Gomez-Rodriguez, J. M.; Colchero, J.; Gomez-Herrero, J.; Baro, A. M. WSXM: a software for scanning probe microscopy and a tool for nanotechnology. *Rev. Sci. Instrum.* **2007**, *78*, 013705.
(111) Miller, S. F.; Friedrich, H. B.; Holzapfel, C. W. The Effects of SCILL Catalyst Modification on the Competitive Hydrogenation of 1-Octyne and 1,7-Octadiene versus 1-Octene. *ChemCatChem* **2012**, *4*, 1337−1344.
(112) Lexow, M.; Talwar, T.; Heller, B. S. J.; May, B.; Bhuin, R. G.; Maier, F.; Steinrück, H. P. Time-dependent changes in the growth of ultrathin ionic liquid films on Ag(111). *Phys. Chem. Chem. Phys.* **2018**, *20*, 12929−12938.
(113) Shirley, D. A. High-Resolution X-Ray Photoemission Spectrum of the Valence Bands of Gold. *Phys. Rev. B* **1972**, *5*, 4709−4714.
(114) Argile, C.; Rhead, G. E. Adsorbed layer and thin film growth modes monitored by Auger electron spectroscopy. *Surf. Sci. Rep.* **1989**, *10*, 277−356.

https://dx.doi.org/10.1021/acs.langmuir.0c02596
Langmuir 2020, 36, 13670−13681